Thermal Stress Analysis of Solid Oxide Fuel Cell with Z-type and Serpentine-type Channels Considering Pressure Drop

Congying Jiang[a,b], Yuchen Gu[a,b], Wanbing Guan[b,*], Meng Ni[c], Junkang Sang[b], Zheng Zhong[a,d,*], Subhash C. Singhal[b]

[a]School of Aerospace Engineering and Applied Mechanics, Tongji University, Shanghai 200092, China

[b]Ningbo Institute of Material Technology and Engineering, Chinese Academy of Sciences, Ningbo 315201, China

[c]Department of Building and Real Estate, The Hong Kong Polytechnic University, Hung Hom, Kowloon, Hong Kong SAR, China

[d] School of Science, Harbin Institute of Technology, Shenzhen 518055, China

Abstract

A thermo-electro-chemo-mechanical coupled 3D model was applied to simulate the performance and thermal stress of a double-sided cathode structured solid oxide fuel cell (DSC-SOFC) with two different air channel configurations: Z-type parallel and triple-parallel serpentine. The distribution of temperature, current density, fuel gas and thermal stress under different voltages in DCS-SOFC was illustrated, and the output power density of the cell was analyzed considering both the electrochemical power and the dissipative power caused by the pressure drop. It was found that the Z-type parallel cell gave a better performance under a low current density, while the triple-parallel serpentine cell was more efficient at a current density higher than 6330 A·m^{-2}. A comparison of thermal stress distributions between the two flow field designs showed a small difference in maximum 1st principle stresses under the same operational

* Corresponding author.

Email address: W.B. Guan, wbguan@nimte.ac.cn; zhongzheng@hit.edu.cn

voltages. Compared to the Z-type parallel flow field, the maximum 1st principle stress in the triple-parallel serpentine was much smaller under the same current density or electrochemical power, while much larger under the same output power.

Keywords: Thermal stress; Channel configuration; Double-sided cathode; Solid oxide fuel cell

1   Introduction

Solid Oxide Fuel Cell (SOFC) is a highly efficient, environmentally friendly and fuel-flexible power generation device.[1] During the past decades, several different geometries of SOFCs have been proposed. Today, commercially available systems are mainly based on the planar configuration due to easy manufacturing, stacking, as well as higher volumetric power densities.[2] For planar SOFC, the proper gas channel design is critical, which can influence both the performance and durability.[3, 4] It is important to ensure the uniformity of species, current density, and temperature in SOFC.[5] Many numerical models have been constructed to investigate the distribution of velocities of gases, concentrations of fuel and oxygen, electrochemical reaction rate, current density, and temperature in SOFC with different gas channel configurations. Liu et al.[6] analyzed the electrochemical performance of SOFC with different gas flow directions (co-, counter- and cross-flow) using a 3D numerical model. The results showed a higher current density for co- and counter-flow (~1%) than for cross-flow. Similarly, Zhang et al.[7] predicted that maximum current density in SOFC is located at the interfaces

between the channels, ribs, and the electrodes. Manglik et al.[8] modeled the mass and heat transfers in SOFC with different gas channel cross sections (rectangular, trapezoidal, and triangular). They found that rectangular gas duct offered improved mass and heat transfer efficiency and better thermal management. Khazaee and Rava[4] studied the SOFC performance of rectangular, trapezoidal, and triangular channel cross sections with rectangular channel showing better performance. Andersson et al. ,[9] by optimizing the cross-section size of channel, showed a considerable increase in volumetric cell current of SOFC for wider and thinner gas channel.

Previously, researchers have mainly focused on the flow direction and cross-section of gas channel in SOFC; however, the shape of flow field is also important.[10-12] Huang and Zhu[13] studied the flow distribution in U-type fuel cells using a CFD model, showing that the flow distribution could be improved by reducing the pressure drop or augmenting the diameter of channel. Danilov and Tade[14] redesigned the inlet anode parallel flow field in a CFD-based SOFC model by optimizing the velocity, temperature, and local current density distribution in anode while ignoring the cathode influence. Huang[15] experimentally measured the velocity distribution and electrochemical performance of SOFC with and without guide vanes. They found that guide vanes help to ensure uniform velocity distributions in SOFC with ~ 10 % power density increment. It was also found that the re-oxidation occurred when the flow field was non-uniform. Kapadia et al. [10] got uniform fuel distribution and improved current density by utilizing a gradient-based optimizer to update the size of parallel channels in Z-type channel.

Jackson et al.[12] increased header widths to optimize flow distribution in order to assess flow maldistribution. Wei et al.[16] showed a 6.3% increment in power density by proposing a new flow channel design. Saied et al.[17] studied the performance of the planar anode-supported SOFC with different flow field designs and triple-entry serpentine showed the best performance. Recently, Xu et al.[18] simulated the performance of SOFC with interdigitated flow channel. The results showed potential application of this design in future; however, experimental verification is still needed.

The effect of flow field design on SOFC performance has been studied during the past decades. However, these studies mainly focused on the electrochemical power while neglecting the power loss caused by pressure drop in channels. In fact, to maintain the gas flow in a channel, pumping power is needed to ensure a higher pressure at the inlet than that at the outlet, which in turn reduces the total output power of SOFC. Thus, the total output power, which is important, of SOFC equals the electrochemical output power of SOFC deducted by the pumping power due to pressure loss in the gas channel. It is necessary to calculate the total output power of SOFC with different channel configurations. In this study, the total output power of DSC-SOFC with two typical channel configurations (Z-type channel and triple-parallel serpentine channel) are simulated and compared. The former configuration was reported to have a smaller pressure drop, while the serpentine channel provided a higher electrochemical power.[12,18] Moreover, some researches were conducted to simulate the thermal stress in SOFC, while most of them investigated the distribution of thermal stress under a certain

condition (such as fixed operation voltage or cell configuration)[19-21]. Detailed study on the stress distribution under different channel shapes or under different operational voltages is still lacking in the literature. In this work, the distributions of thermal stresses in above two typical channel configurations were analyzed and compared, when they were simulated under the same operational voltage, current density, electrochemical power and total output power. In the present work, a thermo-electro-chemo-mechanical coupled theoretical model with different gas channel configurations (Z-type parallel and triple-parallel serpentine) was developed and solved by Comsol multiphysics computer software.[22] The models were validated by comparing the simulation results with experimental data. The performance and the distribution of thermal stresses of different SOFCs were simulated with different operating voltages. The results of this work provide guidance for designing gas channel configuration to achieve high performance and high durability.

2　Model description

The 3D thermo-electro-chemo-mechanical coupled finite element model is developed and takes the gas flow, heat flow, electrochemical reaction, mass/ion/electron transportation, and thermal deformation into consideration. The complicated geometry, governing equations, and boundary conditions used in this model are illustrated in this section.

2.1 Geometry

In this work, the double-sided cathode structure SOFC is employed as shown in fig.1. For this type of SOFC, deformation introduced by thermal stress is partially offset by its completely symmetric structure, which benefits the redox performance of SOFC.[23, 24]
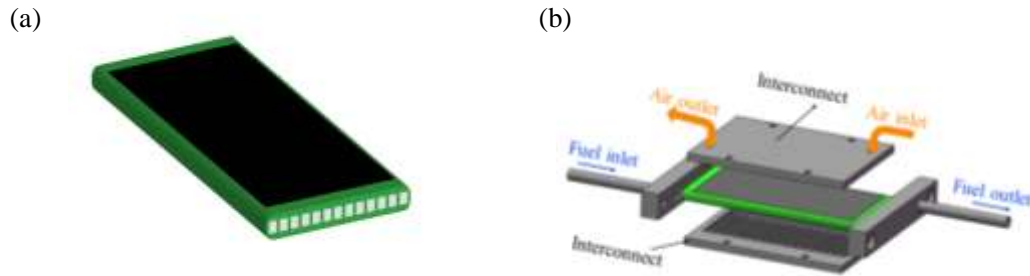
(a) (b)

Fig. 1 Geometry of designed SOFC with double-sided cathodes (a) schematic diagram, (b) schematic of assembly system.

As the double-sided cathodes SOFC is symmetric, only the half-cell is included in the simulation. This model consists of 26 metallic alloy interconnect tips (1.15 mm×28 mm×1 mm), an air channel, a $La_{0.6}Sr_{0.4}Co_{0.2}Fe_{0.8}O_{3-\delta}$ (LSCF) perovskite cathode active layer (85.5 mm×41 mm×0.02 mm), a yttria-stabilized zirconia (YSZ) electrolyte layer (85.5 mm×41 mm×0.01 mm), a NiO+8YSZ anode active layer (85.5 mm×41 mm×0.02 mm), a NiO+3YSZ anode support layer, and 13 fuel gas channels (98.6 mm×2.5 mm×2.3 mm), as shown in Fig. 2a. The schematic geometry of SOFC is shown in Fig. 2b. To illustrate the flow of air more clearly, the geometry of Z-type parallel air channel

is given in Fig. 2c, and the geometry of triple-parallel serpentine air channel is given in
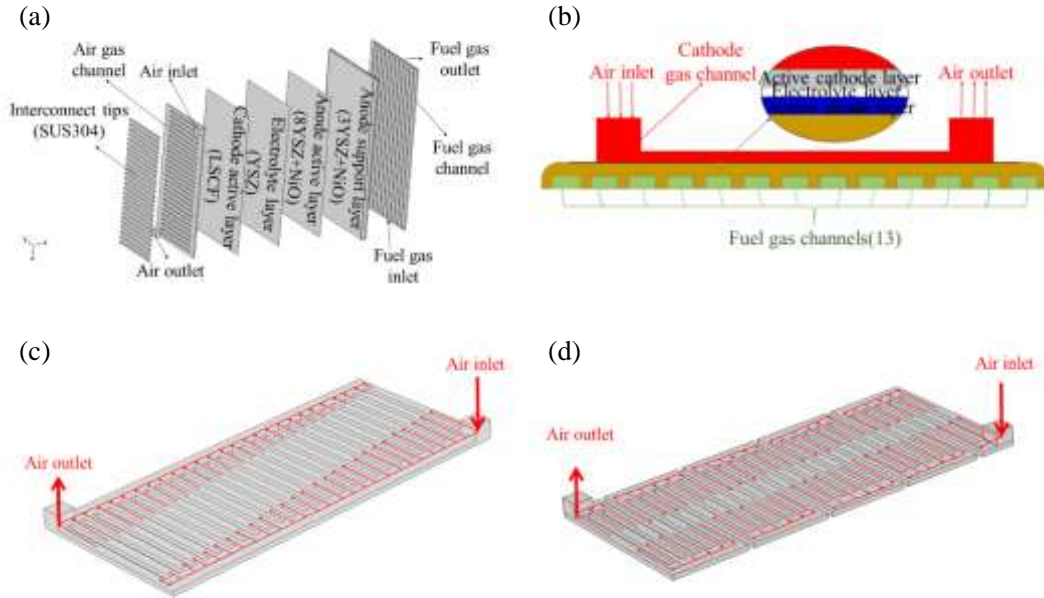
Fig. 2d.

Fig. 2 Geometry of double-sided cathodes SOFC: (a) components of SOFC, (b) overall
geometry, (c) Z-type parallel air gas channel and (d) triple-parallel serpentine air gas channel.

2.2 Governing equations

The 3D thermo-electro-chemo-mechanical coupled numerical model fully

considers the electrochemical reactions, gases flow, species diffusion, heat transfer, and

solids deformation processes. To present these processes clearly, it is necessary to

couple electrochemical reaction models, gas flow models, species diffusion models,

heat transfer model, and mechanical model together. The governing equations of these

models are presented below.

2.2.1 Electrochemical reaction models

Hydrogen oxidation in active anode layer is considered in this work as:

$$H_2 + O^{2-} \rightarrow H_2O + 2e^- \tag{1}$$

where H_2 is supplied by fuel channel and O^{2-} is produced in cathode and transported into anode through the dense electrolyte. At the cathode, one mole O_2 accommodates four moles of electrons at the surface area of LSCF which is exposed to air, as shown in Eq. (2):

$$O_2 + 4e^- \rightarrow 2O^{2-} \tag{2}$$

The operating cell potential (E) from the SOFC can be determined using the equilibrium potential and the various overpotential losses:

$$E = E^{OCV} - \left(\eta_{act} + \eta_{ohm} + \eta_{conc} \right) \tag{3}$$

where E^{OCV} is the equilibrium potential (Nernst potential) when the current density is zero. η_{act}, η_{ohm} and η_{conc} are activation, ohmic and concentration overpotentials, respectively. For the hydrogen-steam mixed fuel, the equilibrium potential can be calculated by the Nernst equation with the standard electrode potential E^0, universal gas constant R, temperature T, pressure p, Faraday's constant F and partial pressure of component i (p^i) [25]:

$$E^{OCV} = E^0 - \frac{RT}{2F} \ln \left(\frac{p^{H_2O}}{p^{H_2} \left(p^{O_2} \right)^{0.5}} \right) \tag{4}$$

In addition, the standard electrode potential E^0 can be expressed as[25]:

$$E^0 = 1.253 - 2.4516 \times 10^{-4} T \tag{5}$$

The activation polarization and current density relationships in anode and cathode are described by the Butler–Volmer (BV) equations, in which both η_{act} and η_{conc} are considered[26-28]:

Anode:
$$i^a = S_{TPB}^a i_0^a \left[\frac{c^{H_2}}{c_{ref}^{H_2}} \exp\left(\frac{\alpha^a n^a F\left(\eta_{act}^a + \eta_{conc}^a\right)}{RT} \right) - \frac{c^{H_2O}}{c_{ref}^{H_2O}} \exp\left(\frac{\left(1-\alpha^a\right)n^a F\left(\eta_{act}^a + \eta_{conc}^a\right)}{RT} \right) \right]$$

Cathode:
$$i^c = S_{TPB}^c i_0^c \left[\exp\left(\frac{\alpha^c n^c F\left(\eta_{act}^c + \eta_{conc}^c\right)}{RT} \right) - \frac{c^{O_2}}{c_{ref}^{O_2}} \exp\left(\frac{\left(1-\alpha^c\right)n^c F\left(\eta_{act}^c + \eta_{conc}^c\right)}{RT} \right) \right]$$

(6)

Where i_0 is the exchange current density (unit); α^a and α^c are the electronic transfer coefficients of anode and cathode, respectively; n is the number of electrons transferred per electrochemical reaction; S_{TPB} (unit) is the triple phase boundary (TPB) length per unit volume; the superscript a and c represent anode and cathode, respectively; c^i is the concentration of component I; η^a_{act} and η^a_{conc} are anode activation and concentration overpotential; η^c_{act} and η^c_{conc} are cathode activation and concentration overpotential.

The activation polarization is related to the ion and electron transport, and also related to the gas-phase partial pressure[25]:

$$\eta_{act}^a = \Phi_e - \Phi_i - E_{eq}^a$$
$$\eta_{act}^c = \Phi_e - \Phi_i - E_{eq}^c$$

(7)

where E^a_{eq} and E^c_{eq} are the equilibrium potentials for anode and cathode, and Φ_e and Φ_i are electric potential of electron and ion. In this work, E^a_{eq} is defined as zero, and E^c_{eq} is set as E^{ocv}.[26,27]

The concentration polarization is caused by the diffusion resistance of the porous media, and can be calculated as[25]:

$$\eta_{conc}^{a} = \frac{RT}{2F} \ln \left(\frac{p_{H_2O,TPB} \cdot p_{H_2,b}}{p_{H_2O,b} \cdot p_{H_2,TPB}} \right)$$

$$\eta_{conc}^{c} = \frac{RT}{2F} \ln \left(\frac{p_{O_2,gc}}{p_{O_2,TPB}} \right) \tag{8}$$

here, b represented the anode surface, g_c represents the cathode surface.

The ohmic overpotential in SOFC is caused by the transfer of ions or electrons. The governing equations for the transport of electrons and ions can be expressed as[29]:

$$\mathbf{i}_i = -\sigma_i^e \nabla \Phi_i$$

$$\mathbf{i}_e = -\sigma_e^e \nabla \Phi_e \tag{9}$$

where, $\mathbf{I}$ and σ^e are the current, conductivity, respectively. The subscript i and e represent ion and electron, respectively, and ∇ is divergence algorithm. Moreover, the ohmic overpotential can be calculated as:

$$\eta_{ohm}^{i} = -\frac{1}{\sigma_i^e} \mathbf{i}_i$$

$$\eta_{ohm}^{e} = -\frac{1}{\sigma_e^e} \mathbf{i}_e \tag{10}$$

where η_{ohm}^i and η_{ohm}^e are ion and electron ohmic overpotentials respectively.

The parameters used in these electrochemical reaction models are summarized in table 1:

Table 1. Values of input parameters for the electrochemical reaction model

Parameters	Value
Effective ionic conductivity of anode (S·m^{-1})[30]	$\dfrac{9.5 \times 10^7}{T} \exp\left(-\dfrac{1150}{T}\right)$
Effective ionic conductivity of cathode (S·m^{-1})[30]	$\dfrac{4.2 \times 10^7}{T} \exp\left(-\dfrac{1200}{T}\right)$
Ionic conductivity of electrolyte (S·m^{-1})[30]	$33.4 \times 10^3 \exp\left(-\dfrac{10300}{T}\right)$
Electronic conductivity of anode (S·m^{-1})[31]	30300
Electronic conductivity of cathode (S·m^{-1})[31]	17000
Electronic conductivity of interconnect (S·m^{-1}) [31]	769000
TPB length per unit volume of anode (m.m^{-3})[33]	2.14×10^5
TPB length per unit volume of cathode (m.m^{-3})[33]	2.14×10^5

Electronic transfer coefficients of anode [34]	0.5
Electronic transfer coefficients of cathode [34]	0.5

2.2.2 Gas flow models

To describe the momentum conservation in porous electrodes as well as gas channels, the widely used Navier-Stokes equation is modified by introducing Darcy's term and the porosity is also considered[28, 34]:

$$\nabla \cdot (\rho \mathbf{v}) = S_{mass}$$

$$\rho \mathbf{v} \cdot \nabla \mathbf{v} = -\nabla p + \nabla \cdot \left[\mu (\nabla \mathbf{v} + \mathbf{v}\nabla) - \frac{2}{3}\mu \nabla \mathbf{v} \right] - \frac{\varepsilon \mu \mathbf{v}}{k}$$

$$\text{Anode}: \qquad S_{mass} = \frac{\left(M_{H_2O} - M_{H_2} \right) i}{2F}$$

$$\text{Cathode}: \qquad S_{mass} = -\frac{M_{O_2} i}{4F}$$

$$(11)$$

where $\mathbf{v}$ is the velocity vector, S_{mass} is the mass source term, ε is the porosity and k is specific permeability which depends on the geometry of the porous medium. ρ and μ are the total gas density and gas dynamic viscosity which are dependent on the component of gas. The values of ρ and μ are calculated with the following equations[35]:

$$\rho = \frac{p \sum x_i M_i}{RT} \tag{12}$$

$$\mu = \sum x_i \mu_i \tag{13}$$

where x_i, M_i and μ_i are the mole fraction, molecular weight and dynamic viscosity of

component i. To get these three parameters, the species diffusion models are needed

and are discussed in the next section.

2.2.3   Species diffusion models

The electrochemical reactions happen near the interface of electrolyte and

electrodes.[36] To reach the reaction sites, gases must diffuse through the pores of the

electrode. The pores in active anode layer are small in comparison with the mean free

path of the gas, which means that molecules collide more frequently with the pore

surfaces and Knudsen diffusion plays an important role in diffusion.[37] Thus, the general

Fick's law which combines Knudsen diffusion and Fick's laws is employed in species

diffusion models:

$$\mathbf{j}_i = -\rho D_i^{mk} \nabla \omega_i - \rho \omega_i D_i^{mk} \frac{\nabla M}{M} + \rho \omega_i D_i^{mk} \sum_k \frac{M_i}{M} \nabla x_i \qquad (14)$$

$$D_i^{mk} = \frac{\varepsilon}{\tau} \left(\frac{1}{D_i^m} + \frac{1}{D_i^k} \right)^{-1} \qquad (15)$$

$$M = \left(\sum_i \frac{\omega_i}{M_i} \right)^{-1} \qquad (16)$$

Here, w_i is mass fraction of specie i, $\mathbf{j}_i$ is the mass flux of species i, ε is the volume

fraction of the pores, τ is the tortuosity factor, M is total molar mass, D^{mk} is total

diffusion coefficient of species which can be calculated by Fick's diffusion coefficient

(D^m) and Knudsen's diffusion coefficient (D^k).[38, 39]

In addition, for the species diffusion models, the conservation of mass is:

$$\nabla \cdot \mathbf{j}_i + \rho \left(\varepsilon \mathbf{v} \cdot \nabla \right) \omega_i = S_i$$

$$S_{H_2} = M_{H_2} \frac{i}{2F}$$

$$S_{H_2O} = -M_{H_2O} \frac{i}{2F} \tag{17}$$

$$S_{O_2} = M_{O_2} \frac{i}{4F}$$

In which S_i is the mass source term of component i which is produced or consumed by electrochemical reaction per second per volume. The change of materials in quantity caused by diffusion (first term), convection (second term) and reaction (third term) are all taken into consideration in Eq. (17).

2.2.4 The heat transfer model

The classical heat transfer governing equation is:

$$\rho C_p \mathbf{v} \cdot \nabla T = \nabla \left(\lambda_{eff} \nabla T \right) + Q \tag{18}$$

where C_p is the specific heat capacity, and Q is the heat source term in the cell. λ_{eff} is the effective thermal conductivity which is determined by the components of gases in gas channels. The λ_{eff} of the porous electrode is calculated as

$$\lambda_{eff} = \left(1 - \varepsilon \right) \lambda_s + \varepsilon \lambda_g \tag{19}$$

where λ_s and λ_g are the thermal conductivity of solids and gases.

In this model, an assumption is made that the heat source is introduced by Joule effect of ions and electrons:

$$Q = \sigma_i^e \nabla \Phi_i \cdot \nabla \Phi_i + \sigma_e^e \nabla \Phi_i \cdot \nabla \Phi_i \tag{20}$$

The parameters used in these gas flow, species diffusion and heat transfer models are presented in table 2:

Table 2. Parameters and values used in the heat and mass transfer models

Parameters	Porosity	Permeability (m^2)	Thermal Conductivity (W·m^{-1}·K^{-1})	Thermal capacity (J·Kg^{-1}·K^{-1})
Anode active layer[7]	0.23	1×10^{-12}	6	450
Anode support layer[7]	0.46	1×10^{-10}	5	400
Electrolyte[7]	-	-	2.7	550
Cathode layer[7]	0.3	1×10^{-12}	11	430
Interconnect[7]	-	-	20	550

2.2.5 *The mechanical model*

The mechanical model in this work assumes that solid materials in SOFC are elastic, and the deformation caused by thermal stress is small. The traditional three-dimensional governing equations can be sorted into three types of equations as[40]:

$$\begin{aligned}
\text{Geometric equation} \quad & \boldsymbol{\varepsilon} = \left(\nabla \mathbf{u} + \mathbf{u} \nabla \right)/2 \\
\text{Momentum equation} \quad & \nabla \cdot \boldsymbol{\sigma} + \mathbf{f} = 0 \\
\text{Constitutive equation} \quad & \boldsymbol{\sigma} = \mathbf{C} : \left(\boldsymbol{\varepsilon} - \boldsymbol{\varepsilon}_{th} \right)
\end{aligned} \tag{21}$$

where $\boldsymbol{\varepsilon}$ and $\boldsymbol{\sigma}$ are two-order tensors which represent total strain and stress respectively. $\boldsymbol{\varepsilon}_{th}$ is the thermal strain. $\mathbf{u}$ is the displacement. $\mathbf{f}$ is body force and $\mathbf{C}$ is a four-order elastic coefficient tensor. For the isotropic materials, the constitutive equation in Eq. (21) can be simplified as:

$$\boldsymbol{\sigma} = \frac{E}{(1+v)(1-2v)}
\begin{bmatrix}
1-v & v & v & 0 & 0 & 0 \\
v & 1-v & v & 0 & 0 & 0 \\
v & v & 1-v & 0 & 0 & 0 \\
0 & 0 & 0 & \dfrac{1-2v}{2} & 0 & 0 \\
0 & 0 & 0 & 0 & \dfrac{1-2v}{2} & 0 \\
0 & 0 & 0 & 0 & 0 & \dfrac{1-2v}{2}
\end{bmatrix}
\begin{bmatrix}
\varepsilon_{xx} \\
\varepsilon_{yy} \\
\varepsilon_{zz} \\
\gamma_{xy} \\
\gamma_{xz} \\
\gamma_{yz}
\end{bmatrix} \tag{22}$$

where E and v are Young's modulus and Poisson's ratio respectively. ε^e_{xx}, ε^e_{yy}, ε^e_{zz}, γ^e_{xy}, γ^e_{xz}, γ^e_{yz} are the longitudinal and shear components for elastic strain. σ_{xx}, σ_{yy}, σ_{zz}, τ_{xy}, τ_{xz}, τ_{yz} are the longitudinal and shear components for stress.

In the thermo-mechanical problem, the thermal strain (ε_{th}) depends on the temperature and CTE with the assumption of isotropy and is given by[41]:

$$\boldsymbol{\varepsilon}_{th} = \alpha \left(T - T_{ref} \right) \mathbf{I} \tag{23}$$

here, T_{ref} (1023K) is the reference temperature under which the cell is considered stress free (The reduction of cell is conducted at 1023K. Due to accelerated creep, the stress is zero at that state).[42, 43] $\mathbf{I}$ is a two-order unit tensor. The parameters used in this

mechanical model are given in table 3:

Table 3. The parameters used in the mechanical model

Layer	Young's modulus (GPa)	Poisson's ratio	CTE ($10^{-6}K^{-1}$)
Anode active layer[44, 45]	220	0.3	12.2
Anode support layer[44, 45]	213	0.3	12.2
Electrolyte[44, 45]	205	0.3	10.3
Cathode layer[44, 45]	30	0.3	12.5
Interconnect[44, 45]	205	0.3	12.3

2.3 Boundary conditions

To simulate the SOFC under working conditions, proper boundary conditions of the cell are necessary. In this work, the laminar flow profile is specified at the gas inlet and the average flow velocities are calculated under different gas flow rates. As for the gas outlet, the pressure is fixed at 1 atm (1.013×10^5 Pa). In addition, the fuel inlet fractions are defined as 0.2% H_2O (mole fraction) and 99.8% H_2, and the volume flow rate is 0.6 L·min^{-1}, which is the same as the experiment. The air inlet is defined as air,

including oxygen (21%, mole fraction) and nitrogen (79%, mole fraction), and the volume flow rate is 5 L·min^{-1} according to the experiment. To simulate the SOFC under the real condition, the initial and boundary temperature are set as 1023K, the same temperature for the gas inlet. The potential at the anode current collector is zero, while the one at metal connector varies from 0.3 V to1.15 V. Moreover, the SOFC is in the stress-free state when it is at the reference temperature (T_{ref}).

3   Results and discussion

3.1   *Distribution of velocity and pressure in air gas channel*

For different channel configurations, the velocities of air in Z-type parallel and triple-parallel serpentine gas channels are different as presented in Fig. 3 when the operational voltage is 1V. For the Z-type parallel gas channel, the flow velocities in 27 parallel channels are non-uniform, which coincides with previously published results.[12] The velocity of air in middle channels flow is much slower than that in channels near the inlet and outlet. The triple-parallel serpentine channel gives uniform velocity distributions in cathode, which benefits the electrochemical performance of SOFC.

(a)   (b)
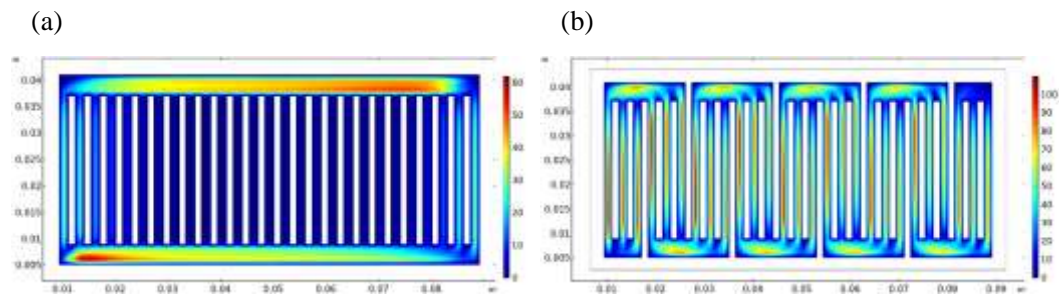
Fig. 3 velocity distribution of air in different gas channels (m·s^{-1}): (a) Z-type parallel, (b) triple-

The distributions of pressure drop in Z-type parallel and triple-parallel serpentine gas channels are shown in Fig. 4 when the operational voltage is 1V. It is noted that the pressure drop in triple-parallel serpentine channel is ten times higher than that in Z-type parallel. This is because the length of triple-parallel serpentine channel is much higher than that in Z-type parallel channel, and the pressure drop increases as the channel length increases.[43] The power loss caused by pressure drop is defined as[47,48]:

$$P_{pd} = q\Delta p \tag{24}$$

where q is the flow rate in channel, Δp is the pressure drop through the gas channel. The power loss increases linearly with the pressure drop and flow rate, and the power loss decreases the total output power of SOFC. In this work, at the flow rate of 5 L·min^{-1}, the power loss caused by pressure drop for Z-type parallel channel (P^Z_{pd}) is about 0.16W, and for triple-parallel serpentine channel (P^S_{pd}) is about 1.80W.

(a)   (b)
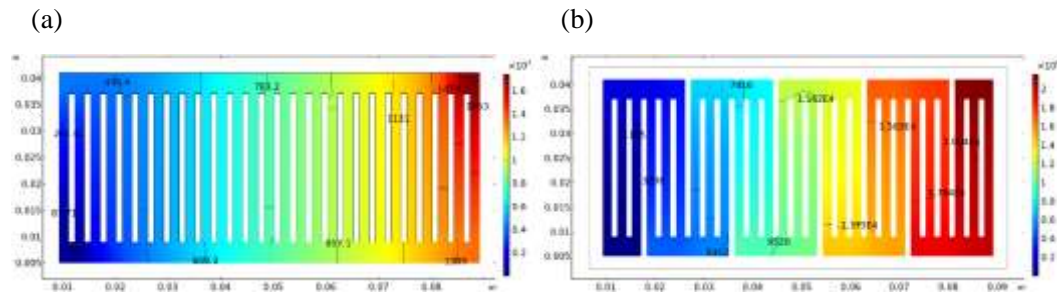
Fig.4 The distribution of pressure drop in different gas channels (Pa): (a) Z-type parallel, (b) triple-parallel serpentine.

3.2   *Mole fraction distribution of gases in cathode*

The distribution of oxygen in cathode is greatly influenced by the flow in air gas channel, and the results above show that the distributions of velocity and pressure in air gas channel are different. Thus, it is necessary to calculate and compare the distribution of gases in cathode with different channel configurations. The mole fractions of oxygen in the middle of cathode layer (10 μm from the interface of cathode and electrolyte) at different operation voltages are illustrated in Fig. 5; the color legends are the same for all cases. For the Z-type parallel gas channel, the distribution of oxygen mole fraction is non-uniform as shown in Fig. 5a and Fig. 5c. Firstly, the velocities of air in the middle parallel channels are smaller than those near the inlet and outlet (illustrated in Fig. 3), and the oxygen consumed by electrochemical reaction cannot be supplied by convection immediately in that area. Thus, the mole fraction of oxygen in cathode layer near middle parallel channels is much smaller, compared with other areas, especially at a low voltage. Secondly, as the air flows from right to left and from up to down, the low oxygen mole fraction area exists at lower left side of middle parallel channels. For the triple-parallel serpentine gas channel, oxygen mole fraction in cathode is well-distributed. The mole fraction of oxygen in cathode layer decreases along the flow direction, and there are no highlighted low oxygen mole fraction areas.
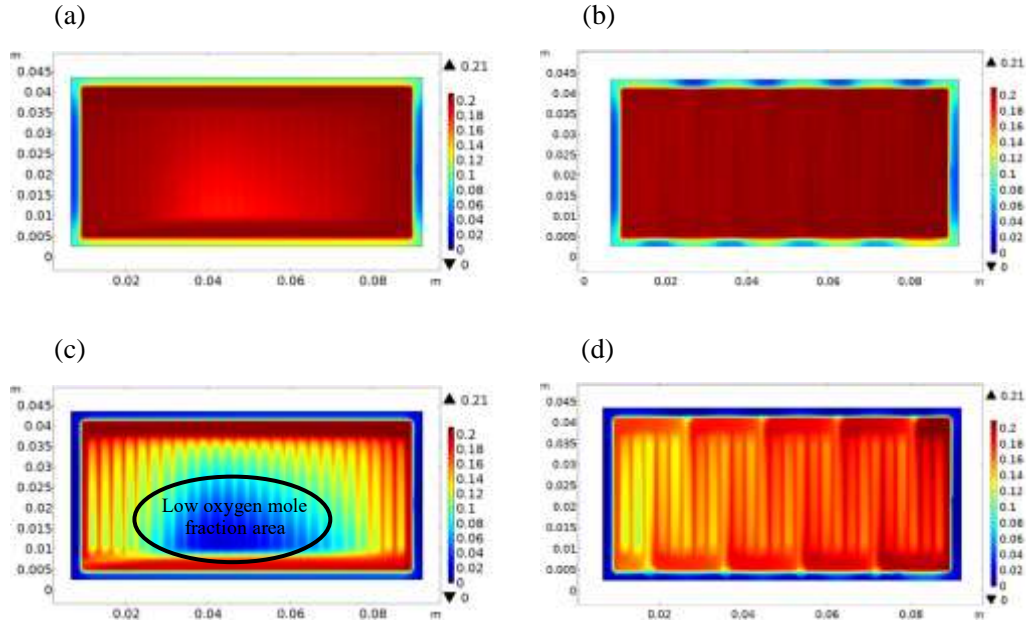
(a)

(b)

(c)

Low oxygen mole
fraction area

(d)

Fig. 5 Mole fractions of oxygen in cathode layer: (a) Z-type parallel, V_{cell}=1V, (b) triple-parallel serpentine, V_{cell}=1V, (c) Z-type parallel, V_{cell}=0.6V, (d) triple-parallel serpentine V_{cell}=0.6V.

3.3 Distribution of current density in electrolyte

The current density in electrolyte is dominated by the rate of electrochemical reaction which is influenced by the voltage, TPB length per unit volume, partial pressure of hydrogen, oxygen and water as expressed in Eq. (6). The partial pressure of oxygen is related to the mole fraction of oxygen in cathode (which is discussed in section 3.2). To understand the impact of mole fraction of oxygen on current density, the distribution of current density in electrolyte is presented and discussed in this section. As presented in Fig. 6, when the voltage decreases from 1V to 0.6V, the current density in electrolyte increases significantly. The fuel gas flows from left to right, as concentration of H_2 in left side is higher than that in right side, and the rate of electrochemical reaction in left side is faster. Moreover, the current density in

21

electrolyte is also influenced by the concentration of oxygen in cathode. For the area where the concentration of oxygen is low in cathode in Fig. 5, the current density in electrolyte is also small.
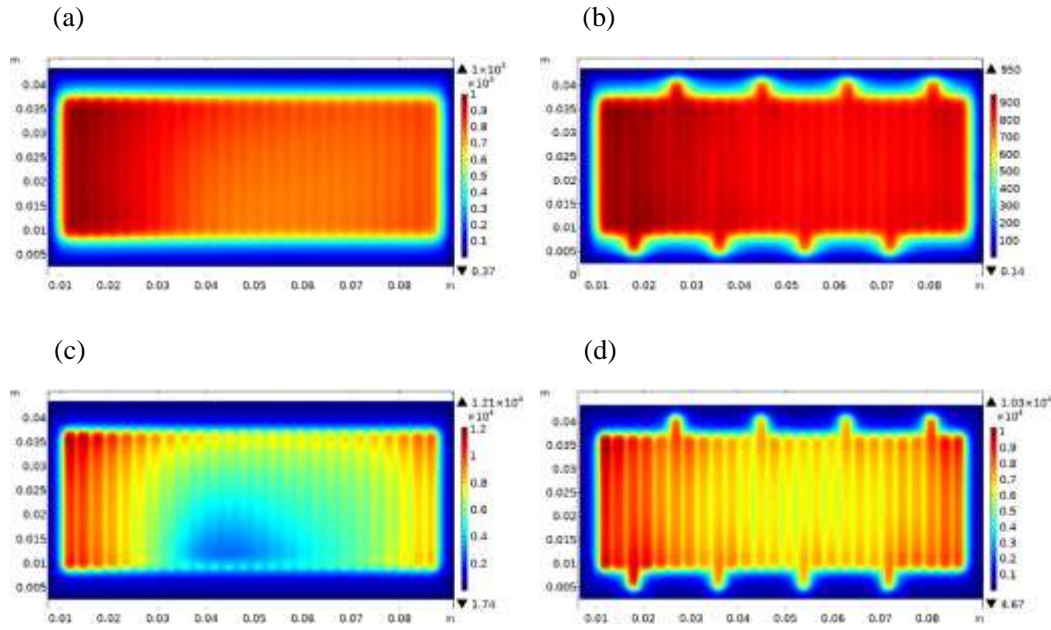

Fig. 6 Distribution of current density in electrolyte (A m^{-2}): (a) Z-type parallel, V_{cell}=1V, (b) triple-parallel serpentine, V_{cell}=1V, (c) Z-type parallel, V_{cell}=0.6V, (d) triple-parallel serpentine V_{cell}=0.6V.

3.4 Electrochemical performance of SOFC

The distribution of current density in electrolyte is revealed in section 3.3, which also dominates the electrochemical performance of SOFC. The current-potential (I-V) characteristics and power density of Z-type parallel and triple-parallel serpentine air gas channel SOFC obtained in simulation are modeled and presented in Fig.7. To validate our model, experiments with Z-type parallel gas channel are carried out, using the Bio-Logic VMP3B-20 electrochemical workstation (France). It shows that the simulation results agree with the experimental data qualitatively and quantitatively. The

power density of SOFC is calculated as:

$$P_{ele} = IV / S_{eff} \tag{25}$$

where I, V, S_{eff} are the total current, operational voltage, and effective electrochemical reaction area, respectively. The electrochemical power density of triple-parallel serpentine gas channel SOFC is higher (especially at the low voltage), because triple-parallel serpentine gas channel gives a higher current density distribution compared to that of the Z-type parallel gas channel. Hence, the triple-parallel serpentine design may succeed in reducing the concentration polarization loss.
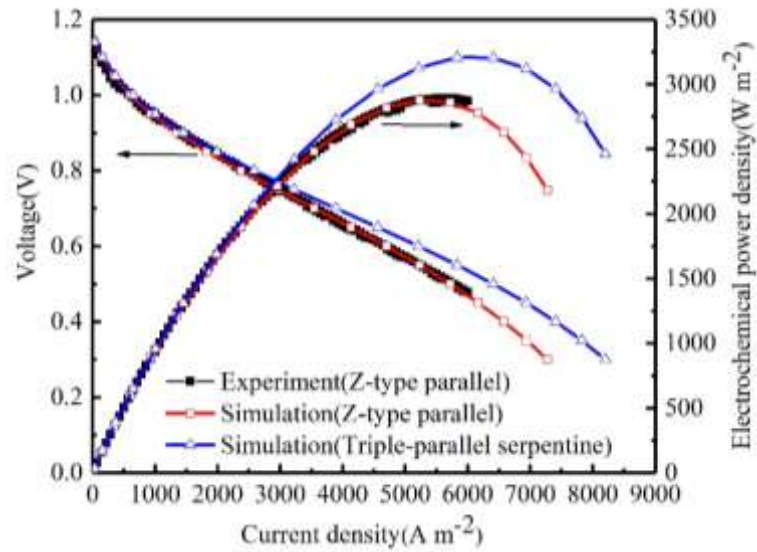
Fig. 7 I-V characteristics and electrochemical power density.

The above results show that triple-parallel serpentine design reduces the concentration polarization losses. In section 3.1, it was found that triple-parallel serpentine design increases the pressure drop power loss. To evaluate the total output power of these two channels, the power loss caused by pressure drop is defined as[47,48]:

$$P_{pd} = \frac{q\Delta p}{\eta_{pump}} \tag{26}$$

where η_{pump} is the pump efficiency. In this work, the pump efficiency is assumed as 1 for simplicity. The power loss increases linearly with the grows of pressure drop and flow rate, and the power loss decreases the total output power of SOFC. The output power density shown in Fig. 8 considers both the electrochemical power density and pressure drop power loss. It is noted that when the current is low, the power consumed by pressure drop is higher than the power generated by the electrochemical reaction, which means that the SOFC needs the external power to maintain the flow of gas in channel, and the output power density is 'negative'. The output power of Z-type parallel SOFC is higher than triple-parallel serpentine when the current density is low. When the current density is higher than 6330 A·m^{-2}, the power loss caused by concentration polarization in Z-type parallel SOFC is higher than the power loss caused by pressure in triple-parallel serpentine SOFC, and the output power in triple-parallel serpentine SOFC is higher than that in Z-type parallel SOFC.
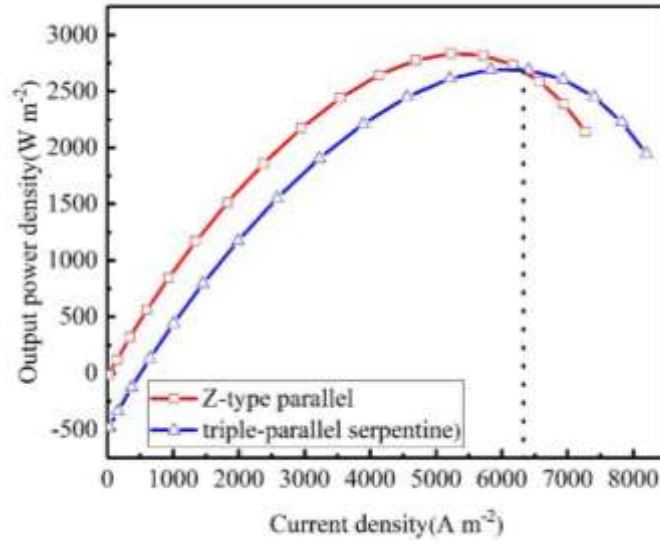
Fig. 8 Output power density vs current density.

3.5 Distribution of temperature in electrolyte

On one hand, the flows of ions and electrons heat up SOFC because of Joule effect as shown in Eq. (20). On the other hand, the heat transfer is also influenced by the flow of gases in Eq. (18). The distributions of electrical and flow fields of SOFCs with different channels are different, and the distribution of temperature is also not the same. The profiles of temperature in SOFC electrolyte are calculated and shown in Fig.9. The high temperature area locates near the fuel inlet and the air output edge, which was also reported by Mastropasqua.[49] The temperature distributions are characterized as highly non-uniform, especially at a low voltage, which may cause local thermal stress and lead to the failure of SOFC. The relation between (average and maximum) temperature and operating voltage in electrolyte is non-linear as illustrated in Fig. 10. Compared with Z-type parallel SOFC, the maximum temperatures in electrolyte in triple-parallel

25

serpentine cells at the same operating voltages are higher because of the stronger Joule heating process introduced by larger current densities. Moreover, the average output air temperatures of triple-parallel serpentine SOFC are higher than Z-type parallel SOFC under the same operating voltages as presented in Fig. 11, which indicates that the convective heat loss in triple-parallel serpentine SOFC is much higher than that in Z-type parallel SOFC. Compared with Z-type parallel SOFC, triple-parallel serpentine SOFC has a stronger Joule heating process and higher convective heat loss. Therefore, the overall average temperatures in electrolyte for two kinds of SOFCs are almost the same as shown in Fig.10.
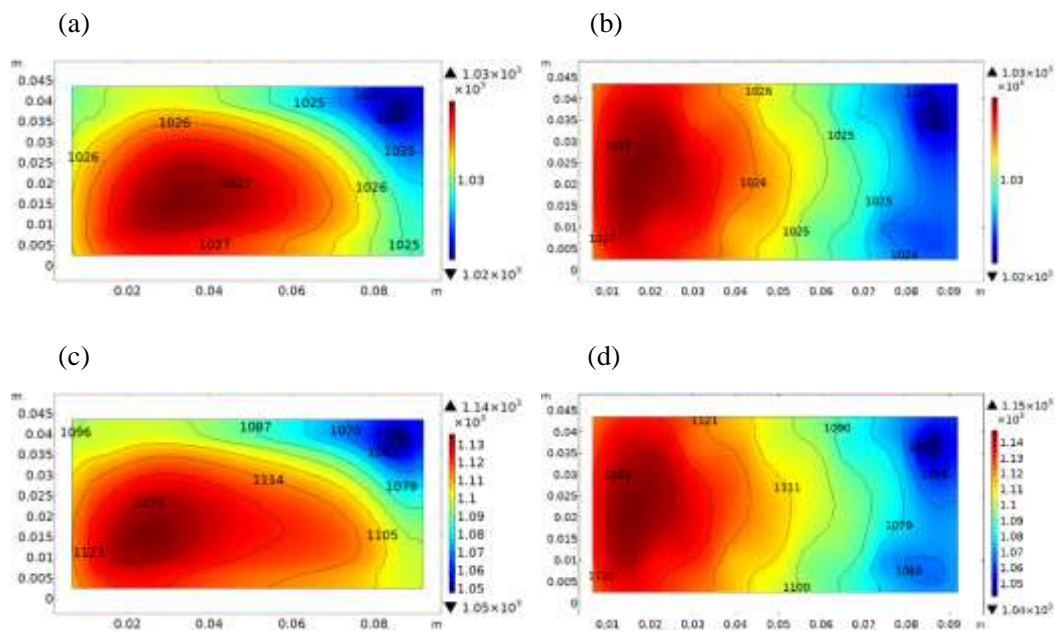

Fig. 9 Distribution of temperature in electrolyte (K): (a) Z-type parallel, V_{cell}=1V, (b) triple-parallel serpentine, V_{cell}=1V, (c) Z-type parallel, V_{cell}=0.6V, (d) triple-parallel serpentine V_{cell}=0.6V.
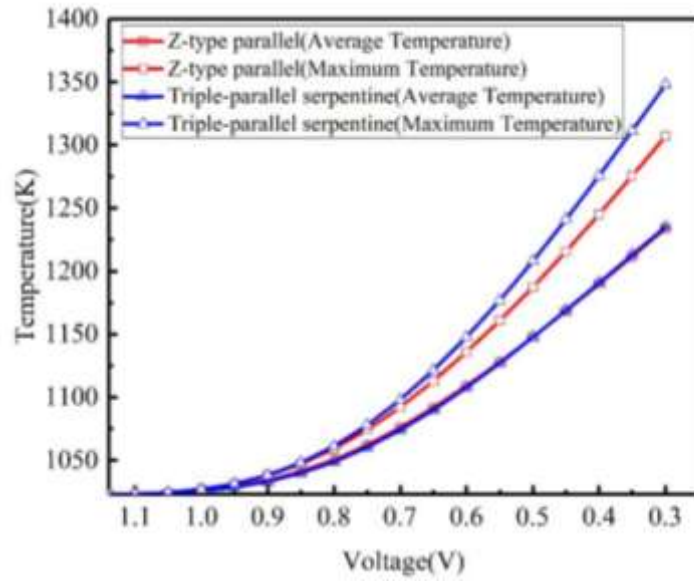
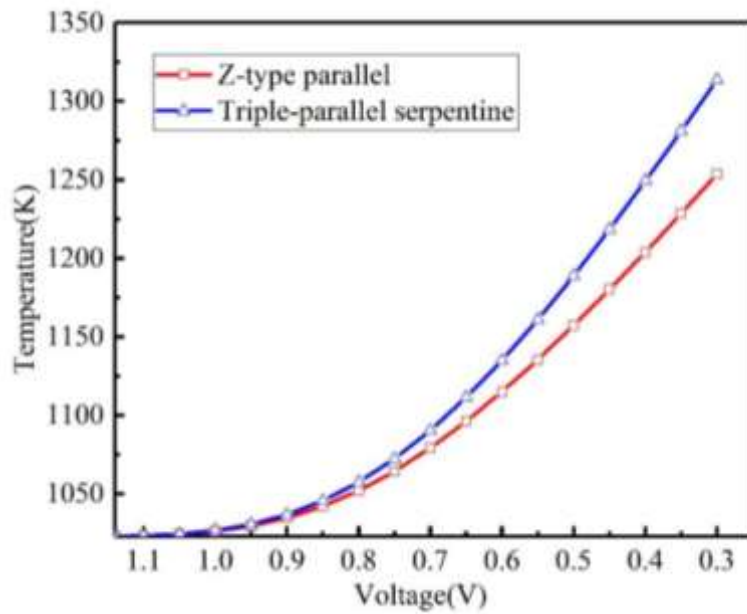Fig. 10 Average and maximum temperature under different voltages in electrolyte.

Fig. 11 The average temperatures of output gas under different voltages.

3.6 Distribution of stress in SOFC

The thermal stress in SOFC is generated by the mismatch of CTE (Coefficient of

Thermal Expansion) and the temperature gradient. Based on the results of temperature distribution in section 3.5, the thermal stress in SOFC is modeled and analyzed. The 1st principal stress is normally the maximum stress normal to a plane which may induce thermal cracks in the ceramic cell, and it is always used to predict the lifetime of a cell and its cracking occurrence. For the SOFC in operation condition, the 1st principal stress in electrolyte is much higher than that in anode and cathode, and the electrolyte is easier to fail because of the high thermal stress.[6] The distribution of 1st principal stress in electrolyte is shown in Fig. 10. It can be seen that the distribution of thermal stress in triple-parallel serpentine SOFC is symmetrical and the maximum stress areas appear at the left up and left down sides in electrolyte, while for the Z-type parallel SOFC, the maximum stress area located at the left down side in electrolyte. The maximum 1st principle stress under different conditions are presented in Fig. 13. When the operating voltages are the same, the difference of maximum 1st principle stresses between these two channel configurations is small. In contrast, the maximum 1st principle stress in triple-parallel serpentine SOFC is much smaller than that in Z-type parallel SOFC under the same current densities or the same electrochemical power densities, as presented in Fig. 13(b) and Fig. 13(c). Thus, for constant current discharge process, the triple-parallel serpentine channel configuration is a better choice. Moreover, Fig. 13(d) reveals that the maximum 1st principle stress in triple-parallel serpentine SOFC is larger than that in Z-type parallel SOFC under the same output powers.
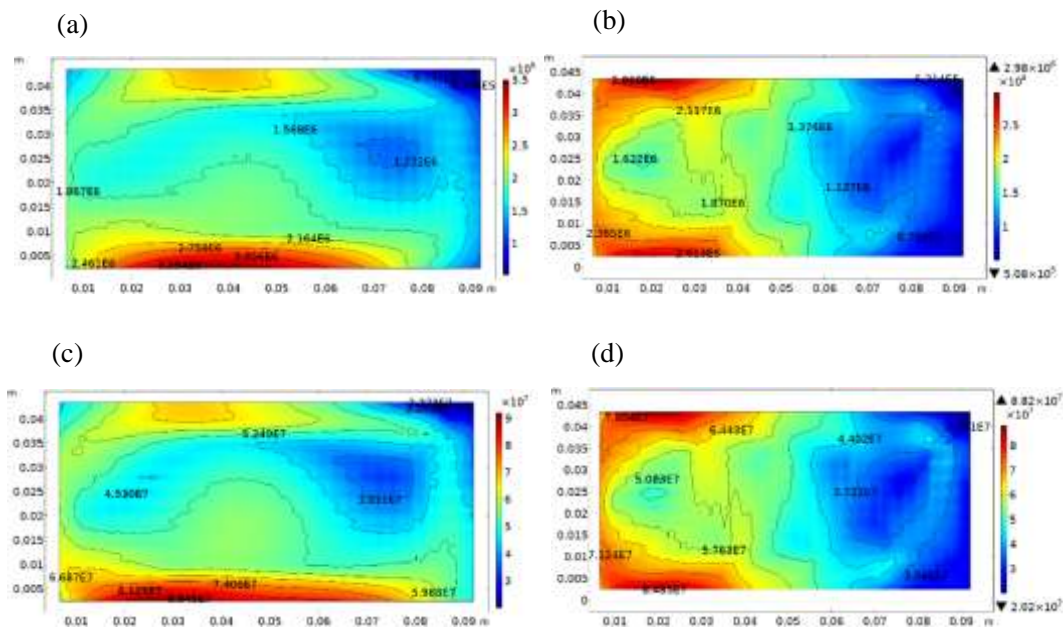
Fig. 12 Distribution of the 1st principal stress in electrolyte (Pa):(a) Z-type parallel, V_{cell}=1V (b) triple-parallel serpentine , V_{cell}=1V, (c) Z-type parallel, V_{cell}=0.6V (d) triple-parallel serpentine , V_{cell}=0.6V.
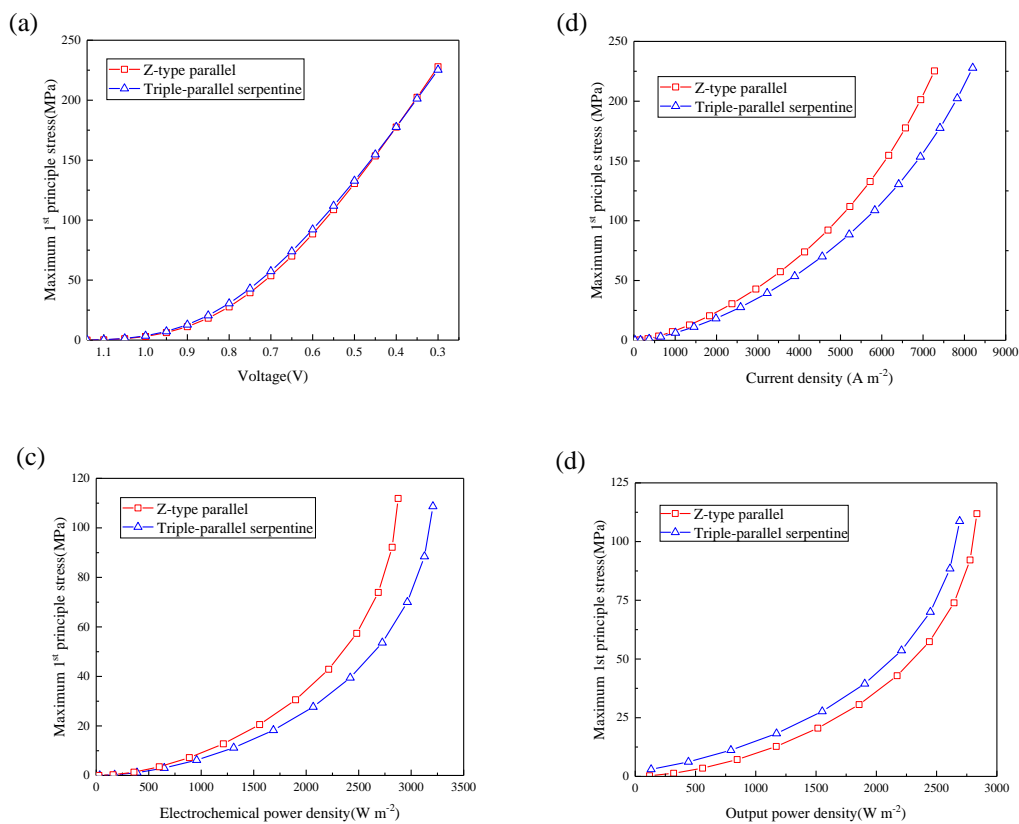

Fig. 13 The maximum 1st principal stresses in SOFC under different conditions: (a) different voltages (b) different current densities (c) different electrochemical power densities (d) different

output powers.

3.7 *Discussion*

The results above explicitly show the distributions of gases, current density, temperature and thermal stress in SOFC, and the model is also validated by comparing the modeled I-V results with experiment results.

On one hand, the pressure drop in Z-type parallel channel is ten times lower than that in triple-parallel serpentine, and the power losses caused by pressure drop in Z-type parallel and the triple-parallel serpentine channel are about 0.16W and 1.8 W, respectively. On the other hand, the electrochemical performance of Z-type parallel SOFC is smaller than that of triple-parallel serpentine SOFC. This is because the flow velocities in Z-type parallel are non-uniform, which results in the low oxygen mole fraction area in cathode and the low current density area in electrolyte. To evaluate the efficiency of these two channels, the output power density is put forward and calculated, which considers both the electrochemical power and the power loss caused by pressure drop. The result shows that when the current density is higher than 6330 A·m^{-2}, Z-type parallel SOFC has a higher output power, while when the current density is smaller than 6330 A·m^{-2}, triple-parallel serpentine SOFC has a better efficiency.

Compared with Z-type parallel SOFC, the maximum temperatures in electrolyte of triple-parallel serpentine SOFC at the same operating voltages are higher because of the stronger Joule heating process. Moreover, triple-parallel serpentine SOFC has higher convective heat loss. Consequently, the overall average temperatures in

electrolyte of these two SOFCs are almost the same.

The distributions of thermal stress in Z-type parallel and the triple-parallel serpentine SOFC are calculated and compared. When the operating voltages are the same, the difference of maximum 1st principle stresses between these two channel configurations is small. The maximum 1st principle stress in triple-parallel serpentine SOFC is much smaller compared with that in Z-type parallel SOFC under the same current densities or the same electrochemical power densities, which indicates that the triple-parallel serpentine channel configuration is a better choice for constant current discharge process. Moreover, the maximum 1st principle stress in triple-parallel serpentine SOFC is larger than that in Z-type parallel SOFC under the same output powers.

4 Conclusions

A comprehensive thermo-electro-chemo-mechanical coupled 3D theoretical model was applied to characterize the performance and thermal stress distributions in DCS-SOFC with Z-type and Serpentine-type channels. In this work, not only the electrochemical performances of SOFC with these two channels are compared, but the power losses caused by pressure drop are also considered. Results show that Z-type parallel SOFC has higher output power with low current density, while triple-parallel serpentine SOFC has better efficiency when the current density is high. Moreover, the distributions of thermal stress in Z-type parallel and the triple-parallel serpentine SOFC

are calculated and compared. The maximum 1st principle stress in triple-parallel serpentine SOFC is smaller than that in Z-type parallel under the same electrochemical powers while larger under the same output power.

Acknowledgements

References

1. S. C. Singhal and K. Kendall, *High-temperature solid oxide fuel cells: fundamentals, design and applications*, Elsevier (2003).

2. H. Yakabe, T. Ogiwara, M. Hishinuma and I. Yasuda, *J. Power Sources*, **102**, 144 (2001).

3. A. Kumar and R. G. Reddy, *J. Power Sources*, **113**, 11 (2003).

4. I. Khazaee and A. Rava, *Energy*, **119**, 235 (2017).

5. C. Jiang, Y. Gu, W. Guan, J. Zheng, M. Ni and Z. Zhong, *Int. J. Hydrogen Energy*, **45**, 1 (2019).

6. S. Liu, W. Kong and Z. Lin, *J. Power Sources*, **194**, 854 (2009).

7. Z. Zhang, D. Yue, G. Yang, J. Chen, Y. Zheng, H. Miao, W. Wang, J. Yuan and N. Huang, *Int. J. Heat Mass Transfer*, **84**, 942 (2015).

8. R. M. Manglik and Y. N. Magar, *J. Therm. Sci. Eng. Appl.*, **7**, 10 (2015).

9. M. Andersson, J. Yuan and B. Sunden, *Fuel Cells*, **14**, 177 (2014).

10. S. Kapadia, W. K. Anderson and C. Burdyshaw, *Comput. Fluids*, **41**, 41 (2011).

11. W. J. Sembler and S. Kumar, *J. Fuel Cell Sci. Technol.*, **8**, 12 (2011).

12. J. M. Jackson, M. L. Hupert and S. A. Soper, *J. Power Sources*, **269**, 274 (2014).

13. W. L. Huang and Q. Zhu, *J. Power Sources*, **178**, 353 (2008).

14. V. A. Danilov and M. O. Tade, *Int. J. Hydrogen Energy*, **34**, 8998 (2009).

15. C. M. Huang, S. S. Shy, H. H. Li and C. H. Lee, *J. Power Sources*, **195**, 6280 (2010).

16. S. S. Wei, T. H. Wang and J. S. Wu, *Energy*, **69**, 553 (2014).

17. M. Saied, K. Ahmed, M. Nemat-Alla, M. Ahmed and M. El-Sebaie, *Int. J. Hydrogen Energy*, **43**, 20931 (2018).

18. Y. Xu, A. Kukolin, D. F. Chen and W. Yang, *Appl. Sci.-Basel*, **9**, 10 (2019).

19. T. L. Jiang and M.-H. Chen, Int. J. Hydrogen Energy, 34, 8223 (2009).

20. X. Fang and Z. Lin, Appl. Energy, 229, 63 (2018).

21. W. Kong, W. Zhang, H. Huang, Y. Zhang, J. Wu and Y. Xu, J Mater Sci Technol, 34, 1436 (2018).

22. A. Comsol, *Version: September*, **10**, 333 (2005).

23. X. Li, Y. Wang, W. Liu, J. A. Wilson, J. Wang, C. Wang, J. Yang, C. Xia, X.-D. Zhou and W. Guan, *Composites Part B: Engineering*, **166**, 549 (2019).

24. W. Liu, Z. Zou, F. Miao, X. Li, J. Wang, J. Yang, J. Wilson, X. Zhou, Z. Zhong and Q. Zhai, *Energy Technology*, **7**, 240 (2019).

25. S. Zeng, G. Yu, J. Parbey, D. Song, T. Li and M. Andersson, *J. Electrochem. Soc.*, **165**, F105 (2018).

26. M. Xu, T. Li, M. Yang and M. Andersson, *Sci Bull (Beijing)*, **61**, 1333 (2016).

27. S. Zeng, X. Zhang, J. Song Chen, T. Li and M. Andersson, *Int. J. Heat Mass Transfer*, **125**, 506 (2018)

28. H. Xu, B. Chen, J. Liu and M. Ni, *Appl. Energy*, **178**, 353 (2016).

29. X. Zhang, J. Parbey, G. Yu, T. Li and M. Andersson, *J. Electrochem. Soc.*, **165**, F1224 (2018).

30. T. N. Chaudhary, U. Saleem and B. Chen, *Int. J. Hydrogen Energy*, **44**, 8425 (2019).

31. P. Pianko-Oprych, T. Zinko and Z. Jaworski, *Materials (Basel)*, **9** (2016).

32. J. W. Stevenson, T. R. Armstrong, R. D. Carneim, L. R. Pederson and W. J. Weber, *J. Electrochem. Soc.*, **143**, 2722 (1996).

33. H. Xu, B. Chen and M. Ni, *J. Electrochem. Soc.*, **163**, F3029 (2016).

34. H. Xu, B. Chen, P. Tan, W. Cai, W. He, D. Farrusseng and M. Ni, *Appl. Energy*, **219**, 105 (2018).

35. S. Zeng, M. Xu, J. Parbey, G. Yu, M. Andersson, Q. Li, B. Li and T. Li, *Int. J. Hydrogen Energy*, **42**, 20239 (2017).

36. M. Hussain, X. Li and I. Dincer, *Int. J. Hydrogen Energy*, **34**, 3134 (2009).

37. F. Yang, J. M. Gu, L. H. Ye, Z. X. Zhang, G. F. Rao, Y. C. Liang, K. C. Wen, J. Y. Zhao, J. B. Goodenough and W. D. He, *Energy*, **95**, 242 (2016).

38. H. M. Yakabe H , Uratani M , et al., *J. Power Sources*, **86(1)**, 423 (2000).

39. K. K. A. Chan S H , Xia Z T, *J. Power Sources*, **93(1-2)**, 130 (2001).

40. Z. B. Kuang, *Theory of Electroelasticity* , Elsevier (2013).

41. X. Jin and X. Xue, *J. Electrochem. Soc.*, **160**, F815 (2013).

42. T. T. Molla, K. Kwok and H. L. Frandsen, *Fuel Cells*, **19**, 96 (2018).

43. H. L. Frandsen, M. Makowska, F. Greco, C. Chatzichristodoulou, D. W. Ni, D. J. Curran, M. Strobl, L. T. Kuhn and P. V. Hendriksen, *J. Power Sources*, **323**, 78 (2016).

44. A. Masini, F. Šiška, O. Ševeček, Z. Chlup and I. Dlouhý, *Int. J. Appl. Ceram. Technol.*, **15**, 370 (2018).

45. M. Xu, T. S. Li, M. Yang, M. Andersson, I. Fransson, T. Larsson and B. Sundén, *Int. J. Hydrogen Energy*, **41**, 14927 (2016).

46. J. Wang and H. Wang, *Fuel Cells*, **12**, 989 (2012).

47. Q. Xu, T. Zhao and P. Leung, Appl. Energy, 105, 47 (2013).

48. C. Blanc and A. Rufer, in 2009 IEEE Energy Conversion Congress and Exposition, p. 2600 (2009).

49. L. Mastropasqua, A. Donazzi and S. Campanari, Fuel Cells, **19**, 125 (2019).